Available online at www.sciencedirect.com
ScienceDirect
Acta Materialia 57 (2009) 993–1003
Acta MATERIALIA
www.elsevier.com/locate/actamat

A sintering model for plasma-sprayed zirconia thermal barrier coatings. Part II: Coatings bonded to a rigid substrate

A. Cipitria, I.O. Golosnoy, T.W. Clyne *

Department of Materials Science & Metallurgy, Cambridge University, Pembroke Street, Cambridge CB2 3QZ, UK

Received 9 July 2008; received in revised form 15 October 2008; accepted 15 October 2008
Available online 29 December 2008

Abstract

The sintering model described in Part I, which relates to free-standing plasma-sprayed thermal barrier coatings, is extended here to the case of a coating attached to a rigid substrate. Through-thickness shrinkage measurements have been carried out for coatings attached to zirconia substrates, and these experimental data are compared with model predictions. The model is then used to explore the influence of the substrate material (zirconia vs. a nickel superalloy), and of the in-plane coating stiffness. Both differential thermal expansion stresses and tensile stresses arising from the constraint imposed on in-plane shrinkage can be relaxed via two diffusional mechanisms: Coble creep and microcrack opening. This relaxation allows progression towards densification, although the process is somewhat inhibited, compared with the case of a free-standing coating. Comparison of the stored elastic strain energy with the critical strain energy release rate for interfacial cracking allows estimates to be made of whether debonding is energetically favoured.[1]

Keywords: Plasma-sprayed thermal barrier coatings; Modelling; Diffusion; Constrained sintering; Variational principle

1. Introduction

The model described in Part I of this pair of papers [1] refers to unconstrained (detached) coatings. Obviously, under service conditions these coatings will remain attached to a substrate. At least in most cases, both the thickness and the stiffness of the coating will be significantly lower than those of the substrate, so that the in-plane dimensions of the coating will be forced to conform to those of the substrate. This naturally affects the progression of the sintering, and the associated changes in properties. It also tends to create residual stresses within the coating, although stress relaxation phenomena are likely to be operative at these elevated temperatures. Of course, stresses can also arise during sintering in the absence of a substrate, for example, as a result of differential shrinkage between different parts, but in general the presence of a rigid substrate is expected to create larger stresses, plus there may be differential thermal contraction effects between substrate and coating as a consequence of changes in temperature.

There have been several previous studies of constrained sintering. For example, Bordia and coworkers published a series of papers [2–6] in the 1980s and 1990s, concerning the mechanisms by which constraint from the presence of a rigid substrate can give rise to stresses and damage, such as crack formation, and also exploring possible constitutive relations describing constrained sintering. Garino and coworkers [7–9] also attempted to quantify the effect of constraint on sintering rates, using essentially empirical relationships. Particular attention has been paid [10,11] to the anisotropic nature of the process and the recent review of Green et al. [12] also highlights this aspect. These treatments were based on the concept of a viscous Poisson coefficient. However, the handling of anisotropy in this way appeared to be rather incomplete and unsatisfactory. The effects of rigid inclusions and heterogeneities on the

* Corresponding author.
E-mail address: twc10@cam.ac.uk (T.W. Clyne).
[1] A compiled version of the sintering model can be downloaded from www.msm.cam.ac.uk/mmc/publications/software.html.

1359-6454/$34.00 © 2008 Acta Materialia Inc. Published by Elsevier Ltd. All rights reserved.
doi:10.1016/j.actamat.2008.10.058

progression of sintering have also been studied [5,13] and there have been several papers oriented towards multi-component and multi-layered systems [14,15], or towards the generation of defects such as cracks [6,14,16].

There have, however, been few attempts to develop sintering models based on the variational principle, in which the effect of constraint is incorporated. The recent paper of Hutchinson et al. [17] is aimed in this direction, but it contains no experimental information, although the modelled microstructure is oriented specifically towards plasma vapour deposited coatings. In the present paper, the theoretical framework outlined in Part I, which relates to a microstructure representative of plasma-sprayed coatings, is extended to encompass the effect of constraint. Comparisons are presented between predictions and experimental data, allowing the validity and limitations of the model to be explored.

2. Experimental procedures

2.1. Production of vacuum plasma-sprayed coatings on zirconia substrates

Samples for constrained sintering experiments were produced by vacuum plasma spraying (VPS) of yttria stabilized zirconia (YSZ) powder, with the composition given in Table 1, onto fully dense zirconia substrates. The higher particle velocities typical of VPS lead to improved coating adhesion. The spraying conditions are listed in Table 2. Technox 2000 zirconia tiles (Dynamic-Ceramic Ltd.) were employed, with dimensions $50 \times 50 \times 5$ mm^3 and a composition of 3 mol.% YSZ (tetragonal). They were grit blasted with alumina, in order to increase the surface roughness and promote coating adhesion. A thermocouple was spot welded onto a metallic plate, which was cemented to the back of the tile. The tile was preheated to about 600 °C immediately prior to spraying. Sintering experiments were carried out both on specimens cut from the sprayed tile and also on detached coatings obtained from the same sprayed material.

2.2. Dilatometry

Dilatometry was carried out in the through-thickness direction, on specimens attached to zirconia substrates, in air at 1400 °C. Dimensional changes were monitored using a DIL 402C Netzsch pushrod dilatometer. The through-thickness shrinkage of free-standing VPS and APS coatings was also measured. (Spraying conditions are given in Table 2.)

Table 2
VPS and APS spraying conditions.

	VPS	APS
Chamber pressure (mbar)	200 (Ar)	Atmospheric
Substrate temperature (°C)	~600	~200
Plasma gun type	F4 (Plasma Technik VPS)	9 MB (Sulzer Metco Plasma System)
Nozzle diameter (mm)	8	6
Plasma gas flow rates (l min^{-1})	Ar, 50 H_2, 8	N_2, 35.4 H_2, 8
Carrier gas flow rates (l min^{-1})	Ar, 4	N_2, 5.2
Arc current (A)	750	500
Voltage (V)	50	78.6
Power (kW)	37.5	39.3
Stand-off distance (mm)	400 (preheat) 250 (spraying)	114

2.3. Microstructural examination

Microstructural examinations were carried out as detailed in Part I. It should be noted that the microstructure of the VPS coatings was rather different from that of the APS coatings shown in Part I. This is illustrated by Fig. 1, which shows low and high magnification views. It can be seen in Fig. 1b that the splat structure is rather finer than that of the APS coatings (see Fig. 1 in Part I), both in terms of the splat thickness and, particularly, in terms of typical spacing between inter-splat contact points.

3. Constrained sintering model framework

An extension to the nomenclature of Part I is shown in Table 3.

3.1. Model geometry

The model geometry of Part I is also employed here, with the additional constraint that the coating is attached to a flat, rigid substrate of infinite extent in the in-plane directions (i.e. the in-plane dimensions are much greater than the coating thickness and there are no edge effects). In the predictions presented here, the substrate is either zirconia or a nickel superalloy, with the possibility of differential thermal contraction misfit strains being absent in the first case and present in the second. The model concerns isothermal sintering, with no thermal gradients present and no externally applied forces or bending moments. It therefore relates to homogeneous constrained sintering, with uniform strain and stress fields through the thickness of the coating, no strain gradients or specimen curvatures and no strains or stresses in the substrate (due to its substantially greater stiffness and thickness).

Table 1
Chemical composition (wt.%) of powder supplied by Sulzer Metco Inc.

ZrO_2	Y_2O_3	SiO_2	Al_2O_3	CaO	Fe_2O_3	HfO_2	MgO	Th	TiO_2	U
Rem.	7.41	0.02	0.07	<0.01	<0.01	1.62	<0.01	<0.002	0.08	<0.002

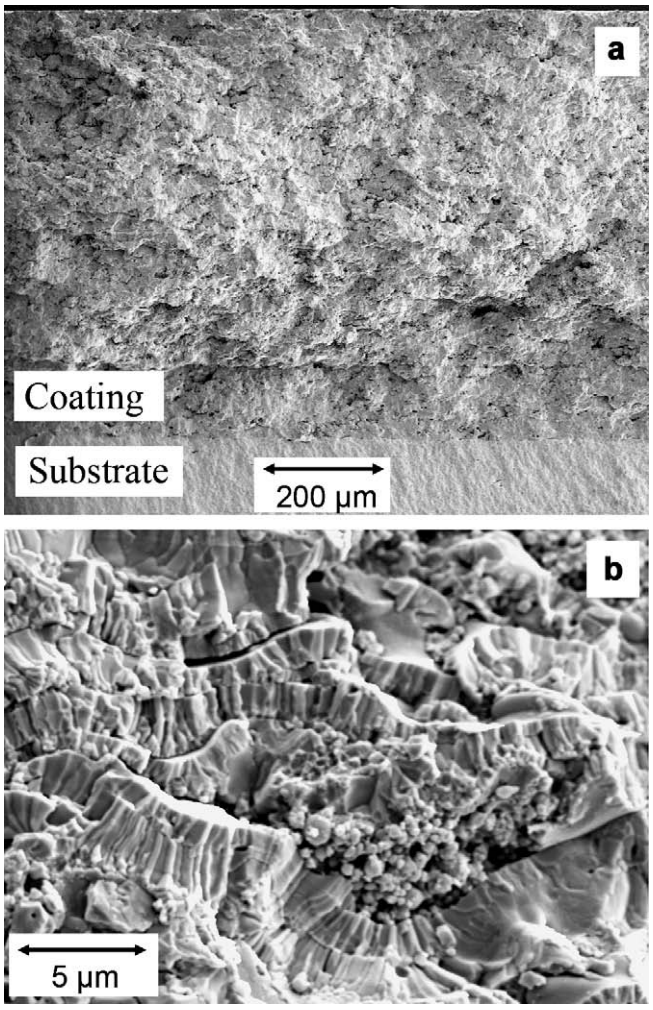

Fig. 1. SEM micrographs of fracture surfaces of as-sprayed YSZ coatings, produced by VPS spraying onto a zirconia substrate, with (a) low and (b) high magnifications.

3.2. Formulation of the variational principle

3.2.1. Free energy of the system

The (rigid) substrate inhibits in-plane dimensional changes. However, sintering still proceeds and, driven by free energy reduction, microstructural changes can take place and can modify the relaxed (stress-free) dimension in the in-plane direction, as well as in the through-thickness direction. Relaxed and actual in-plane coating dimensions can differ, so that in-plane stresses are present (see Fig. 2), but there are no through-thickness stresses. Moreover, if substrate and coating are of dissimilar materials, a thermal expansion mismatch strain may also be generated during temperature change (Fig. 2). The stored elastic strain energy increases the free energy of the system. For a coating with fully interconnected porosity, no contribution to the free energy arises from the pressure acting on free surfaces, and the free energy per unit volume of material, G, is given by

Table 3
Nomenclature of additional symbols for the constrained sintering model (see Part I for other symbols).

Symbol	Units	Meaning
E	Pa	Young's modulus
G_{ic}	J m^{-2}	Critical interfacial strain energy release rate
U	J m^{-3}	Stored strain energy per unit volume of material
α	°C^{-1}	Thermal expansion coefficient
ε	–	Strain
ν	–	Poisson's ratio
σ	Pa	Stress
Superscripts		
E		Elastic
S		Due to constrained sintering
T		Due to thermal expansion mismatch
Subscripts		
av		Averaged
coat		Coating
subs		Substrate
λ		Associated with interfaces (free surfaces and grain boundaries)

$$G = U^E + G_\lambda = \frac{1}{V}\left[\overbrace{\int_V \left[\int_0^{\varepsilon_{kl}} \sigma_{ij}\mathrm{d}\varepsilon_{ij}\right]\mathrm{d}V}^{\text{Stored elastic strain energy}} + \overbrace{\int_{A_S}\gamma_S \mathrm{d}A_S + \int_{A_{gb}}\gamma_{gb}\mathrm{d}A_{gb}}^{\text{Interfacial free energy}}\right] \quad (1)$$

where U^E is the stored elastic strain energy per unit volume of material, G_λ is the free energy per unit volume of material, associated with interfaces (free surface and grain boundaries), and is the same as that for a free-standing coating [1], V is the volume of the material corresponding to a modelled domain, A_S and A_{gb} are the total free surface and grain boundary areas, respectively, and γ_S and γ_{gb} are the surface and grain boundary energies.

The in-plane elastic strain (relative difference between stress-free and actual dimensions) is the sum of the (time-dependent) strain due to constrained sintering $-\varepsilon^S(t)$ (see Fig. 2b) and the (time-independent) thermal expansion mismatch strain, $-\varepsilon^T$ (see Fig. 2a). This net strain, which is assumed isotropic (equal biaxial), is given by

$$\varepsilon^E(t) = -\varepsilon^T - \varepsilon^S(t) = -(\alpha_{coat} - \alpha_{subs})(T - T_D) - \varepsilon^S(t) \quad (2a)$$

where α_{coat} and α_{subs} are the thermal expansivities of coating and substrate, respectively, and T_D, the deposition temperature, is taken as a reference temperature defining the stress-free state. A value of 200 °C is assumed here for T_D, although it should be recognized that in reality it is likely to change with time, since differential thermal contraction misfit stresses can be relaxed, as well as those from sintering. Expressed in terms of the geometrical parameters of the model, the in-plane elastic strain can be written

$$\varepsilon^E_{ip}(t) = -\varepsilon^T - \varepsilon^S(t) = -\left((\alpha_{coat} - \alpha_{subs})(T - T_D) + \frac{r_s(t) - r_{s0}}{r_{s0}} + \frac{a(t) - a_0}{a_0}\right) \quad (2b)$$

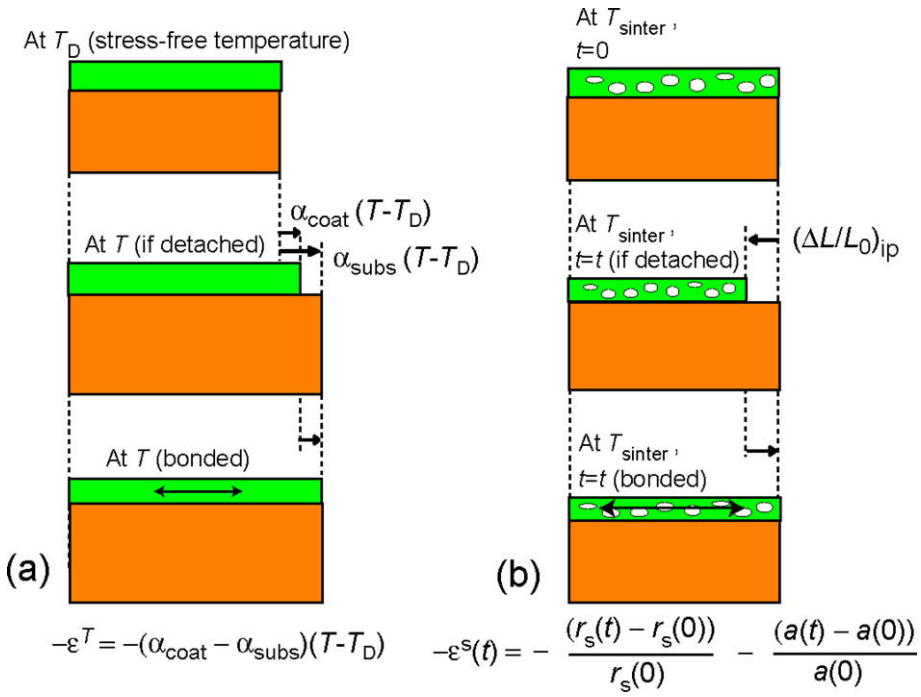

Fig. 2. Schematic representations of elastic strains arising from: (a) thermal expansion misfit and (b) constrained sintering.

while the through-thickness shrinkage is given by

$$\left(\frac{\Delta L}{L_0}\right)_{tt} = -\frac{h(t) - h_0}{h_0} \tag{2c}$$

An averaged uniform stress, σ_{av}, is assumed to be present throughout the coating, so that any local stress variations, such as those due to the presence of pores and microcracks, are neglected. There are no in-plane shear stresses or through-thickness normal stresses. Similarly, an averaged (macroscopic) value is assumed for the in-plane Young's modulus of the coating, E_{av}. Since the stress state is an equal biaxial one, the relationship between the in-plane stress and the associated in-plane strain can be written

$$\sigma_{av}(t) = \frac{E_{av}}{1-\nu}\varepsilon^E(t) \tag{3}$$

where ν is the Poisson's ratio of the coating (assumed isotropic). The effect of different values of E_{av} is investigated here, but its value is assumed to remain constant during sintering. This is a limitation of the current formulation, since it is known that the stiffness tends to increase during sintering [18–23].

The averaged in-plane stress and strain are integrated over the total volume of the system, V_T, which includes the volume of the material, V, and the volume of the voids. The stored elastic strain energy per unit volume of material is given by

$$U^E(t) = \frac{1}{V}\int_{V_T}\frac{E_{av}}{(1-\nu)}(\varepsilon^E(t))^2 \mathrm{d}V = \frac{1}{[1-P(t)]}\frac{E_{av}}{(1-\nu)}(\varepsilon^E(t))^2 \tag{4}$$

where $P(t)$ is the overall porosity.

3.2.2. Rate of energy dissipation

The rate of energy dissipation per unit volume of material, Ψ, during the microstructural evolution of a coating on a substrate, is treated in a similar way to the free-standing case [1], so that there are contributions from diffusion along grain boundaries and free surfaces and from grain boundary migration

$$\Psi = \frac{1}{V}\left[\overbrace{\int_{A_{gb}}\frac{1}{2M_{gb}\Omega\delta_{gb}}(j_{gb})^2\mathrm{d}A_{gb}}^{\text{Grain boundary diffusion}} + \overbrace{\int_{A_S}\frac{1}{2M_S\Omega\delta_S}(j_S)^2\mathrm{d}A_S}^{\text{Surface diffusion}} + \overbrace{\int_{A_{gb}}\frac{1}{2m_m}(v_m)^2\mathrm{d}A_{gb}}^{\text{Grain boundary migration}}\right] \tag{5}$$

where M is the atomic mobility, Ω is the volume per lattice site associated with a diffusing species, j is the volumetric flux per unit length (along an interface), δ is the thickness of the layer through which diffusion takes place, m_m is the grain boundary mobility and v_m is the grain boundary migration velocity. Calculation of the diffusion fluxes and grain boundary migration rate is carried out in a similar way to that outlined in Part I.

One difference with respect to the free-standing case, however, is that diffusion along grain boundaries can be reversed in direction, in order to relax the in-plane tensile stress. This mechanism is essentially Coble creep. Furthermore, if the stress is high enough, the reversed grain boundary diffusion can result in opening of the microcracks.

Lattice diffusion and grain deformation by Nabarro–Herring creep, are, however, omitted from the present formulation, since it seems likely that they can be neglected.

3.2.3. Final equations

The system progresses so as to minimize a function Π, combination of the rate of free energy reduction, $\dot{G}$, and the energy dissipation rate, Ψ

$$\Pi\left(\dot{h},\dot{z}_s,\dot{r}_s,\dot{N}_s,\dot{a},\dot{y}_c\right) = \frac{\mathrm{d}G}{\mathrm{d}t}\left(\dot{h},\dot{z}_s,\dot{r}_s,\dot{N}_s,\dot{a},\dot{y}_c\right) + \Psi\left(\dot{h},\dot{z}_s,\dot{r}_s,\dot{N}_s,\dot{a},\dot{y}_c\right) \tag{6}$$

The minimum occurs at a stationary point of the function Π [17,24–26], such that

$$\delta\Pi = \delta\left(\dot{G}+\Psi\right) = 0 \tag{7}$$

Eq. (7) represents a linear system of six ordinary differential equations, which can be written in matrix form

$$\begin{pmatrix} \frac{\partial^2\Psi^{(1)}}{\left(\partial\dot{h}\right)^2} & \frac{\partial^2\Psi^{(1)}}{\partial\dot{h}\partial\dot{z}_s} & \frac{\partial^2\Psi^{(1)}}{\partial\dot{h}\partial\dot{r}_s} & 0 & 0 & 0 \\ \frac{\partial^2\Psi^{(1)}}{\partial\dot{h}\partial\dot{z}_s} & \frac{\partial^2\Psi^{(1)}}{\left(\partial\dot{z}_s\right)^2} & \frac{\partial^2\Psi^{(1)}}{\partial\dot{z}_s\partial\dot{r}_s} & 0 & 0 & 0 \\ \frac{\partial^2\Psi^{(1)}}{\partial\dot{h}\partial\dot{r}_s} & \frac{\partial^2\Psi^{(1)}}{\partial\dot{z}_s\partial\dot{r}_s} & \frac{\partial^2\Psi^{(1)}}{\left(\partial\dot{r}_s\right)^2} & 0 & 0 & 0 \\ 0 & 0 & 0 & \frac{\partial^2\Psi^{(1)}}{\left(\partial\dot{N}_s\right)^2} & 0 & 0 \\ 0 & 0 & 0 & 0 & \frac{\partial^2\Psi^{(2)}}{\left(\partial\dot{a}\right)^2} & \frac{\partial^2\Psi^{(2)}}{\partial\dot{a}\partial\dot{y}_c} \\ 0 & 0 & 0 & 0 & \frac{\partial^2\Psi^{(2)}}{\partial\dot{a}\partial\dot{y}_c} & \frac{\partial^2\Psi^{(2)}}{\left(\partial\dot{y}_c\right)^2} \end{pmatrix} \begin{pmatrix} \dot{h} \\ \dot{z}_s \\ \dot{r}_s \\ \dot{N}_s \\ \dot{a} \\ \dot{y}_c \end{pmatrix} = -\begin{pmatrix} \frac{\partial\left(\frac{\mathrm{d}G_\lambda^{(1)}}{\mathrm{d}t}\right)}{\partial\dot{h}} + \frac{\partial\left(\frac{\mathrm{d}U^E}{\mathrm{d}t}\right)}{\partial\dot{h}} \\ \frac{\partial\left(\frac{\mathrm{d}G_\lambda^{(1)}}{\mathrm{d}t}\right)}{\partial\dot{z}_s} + \frac{\partial\left(\frac{\mathrm{d}U^E}{\mathrm{d}t}\right)}{\partial\dot{z}_s} \\ \frac{\partial\left(\frac{\mathrm{d}G_\lambda^{(1)}}{\mathrm{d}t}\right)}{\partial\dot{r}_s} + \frac{\partial\left(\frac{\mathrm{d}U^E}{\mathrm{d}t}\right)}{\partial\dot{r}_s} \\ \frac{\partial\left(\frac{\mathrm{d}G_\lambda^{(1)}}{\mathrm{d}t}\right)}{\partial\dot{N}_s} + \frac{\partial\left(\frac{\mathrm{d}U^E}{\mathrm{d}t}\right)}{\partial\dot{N}_s} \\ \frac{\partial\left(\frac{\mathrm{d}G_\lambda^{(2)}}{\mathrm{d}t}\right)}{\partial\dot{a}} + \frac{\partial\left(\frac{\mathrm{d}U^E}{\mathrm{d}t}\right)}{\partial\dot{a}} \\ \frac{\partial\left(\frac{\mathrm{d}G_\lambda^{(2)}}{\mathrm{d}t}\right)}{\partial\dot{y}_c} + \frac{\partial\left(\frac{\mathrm{d}U^E}{\mathrm{d}t}\right)}{\partial\dot{y}_c} \end{pmatrix} \tag{8}$$

The additional terms due to constrained sintering, related to U^E derivatives, are listed in Table 4. The components of the matrix and the vector on the right-hand side depend on the generalized coordinates $(h, z_s, r_s, N_s, a, y_c)$, but not on the generalized velocities $(\dot{h},\dot{z}_s,\dot{r}_s,\dot{N}_s,\dot{a},\dot{y}_c)$. The matrix is symmetric and non-singular, so it can be inverted algebraically. The linear system of ordinary differential equations is solved numerically, using the fourth-order Runge–Kutta method.

Table 4
Additional terms in Eq. (8) associated with constrained sintering (see Part I for other terms).

Stored elastic strain energy	
$\frac{\partial\left(\frac{\mathrm{d}U^E}{\mathrm{d}t}\right)}{\partial\dot{h}} = \left(\frac{E_{av}}{1-\nu}\left(\varepsilon^E\right)^2 B_1\right)$	
$\frac{\partial\left(\frac{\mathrm{d}U^E}{\mathrm{d}t}\right)}{\partial\dot{z}_s} = 0$	$B_1 = \frac{V^{(1)}}{(1-P)^2 r_s^2 h^2}$
$\frac{\partial\left(\frac{\mathrm{d}U^E}{\mathrm{d}t}\right)}{\partial\dot{r}_s} = \left(\frac{E_{av}}{(1-\nu)}\left(\varepsilon^E\right)^2 B_2 + \frac{1}{(1-P)}\frac{E_{av}}{(1-\nu)}B_4\right)$	$B_2 = \frac{2V^{(1)}}{(1-P)^2 r_s^3 h}$
$\frac{\partial\left(\frac{\mathrm{d}U^E}{\mathrm{d}t}\right)}{\partial\dot{N}_s} = 0$	$B_3 = \frac{2V^{(2)}}{(1-P)^2 a^2 L_0 z_{s0}}$
$\frac{\partial\left(\frac{\mathrm{d}U^E}{\mathrm{d}t}\right)}{\partial\dot{a}} = \left(\frac{E_{av}}{(1-\nu)}\left(\varepsilon^E\right)^2 B_3 + \frac{1}{(1-P)}\frac{E_{av}}{(1-\nu)}B_5\right)$	$B_4 = -\frac{2}{r_{s0}}\varepsilon^E$
$\frac{\partial\left(\frac{\mathrm{d}U^E}{\mathrm{d}t}\right)}{\partial\dot{y}_c} = 0$	$B_5 = -\frac{2}{a_0}\varepsilon^E$

4. Model predictions and comparisons with experimental data

The input data relating to the pore geometry are listed in Table 5. In addition to the material property data used with the free-standing model (Part I), further data needed for the constrained sintering model are given in Table 6. Predictions are presented for coatings attached to zirconia or nickel-based superalloy substrates and the effect of different (constant) values of the in-plane coating stiffness is investigated.

4.1. Through-thickness shrinkage

Comparisons presented between theory and experiments are limited for the constrained case to the through-thickness shrinkage of coatings attached to zirconia substrates (since metallic substrates would tend to melt and/or react with the coating if heat treated isothermally). Fig. 3 shows predicted and measured through-thickness shrinkage plots for detached APS, detached VPS and attached VPS coatings. It can be seen from the plots for the two detached coatings that the finer microstructure of the VPS coatings leads to more rapid shrinkage than for APS coatings. The predicted plots capture this effect. The plots for (identical) VPS coatings, attached and detached, show that the (in-plane) constraint leads to an acceleration of the through-thickness shrinkage rate. Again, the predicted curves show similar trends to those observed experimentally, with the assumed coating stiffness of 20 GPa corresponding to typical measured values for these coatings in the as-sprayed state [23]. While this comparison is necessarily limited, it does suggest that the model is capturing the main features of the behaviour. The minor discrepancies between observed and predicted plots can be attributed to experimental error and the simplifications incorporated in the model. (It may be noted that running the constrained model with E_{coat} set to zero is equivalent to the detached case, since no stresses will be generated in the coating under these conditions.)

Table 5
Model input data for pore geometry.

	Unit	Monosized (APS)	Bimodal (APS)		Bimodal (VPS)	
Inter-splat pores						
z_{s0}	m	1.25×10^{-6}	1.25×10^{-6}	1.25×10^{-6}	1.00×10^{-6}	1.00×10^{-6}
h_0	m	1.313×10^{-6}	1.275×10^{-6}	1.350×10^{-6}	1.025×10^{-6}	1.100×10^{-6}
r_{s0}	m	3.00×10^{-6}	3.00×10^{-6}	3.00×10^{-6}	2.10×10^{-6}	2.10×10^{-6}
r_{b0}	m	1.162×10^{-6}	1.162×10^{-6}	1.162×10^{-6}	8.133×10^{-7}	8.133×10^{-7}
g_0	m	5.00×10^{-7}	5.00×10^{-7}	5.00×10^{-7}	5.00×10^{-7}	5.00×10^{-7}
$b_0 = 2(h_0 - z_{s0})$	m	125×10^{-9}	50×10^{-9}	200×10^{-9}	50×10^{-9}	200×10^{-9}
$(h - z_s)^{-1}$	m^{-1}	1.6×10^{7}	4.0×10^{7}	1.0×10^{7}	4.0×10^{7}	1.0×10^{7}
$(A_b/A_T)_0 \propto (r_{b0}/r_{s0})^2$	%	15	15	15	15	15
P	%	4.05	1.67	6.30	2.07	7.73
S	$m^2\ m^{-3}$	6.88×10^{5}	6.83×10^{5}	6.92×10^{5}	8.56×10^{5}	8.74×10^{5}
Intra-splat microcracks						
a_0	m	3.75×10^{-6}	3.75×10^{-6}	3.75×10^{-6}	3.75×10^{-6}	3.75×10^{-6}
y_{c0}	m	3.688×10^{-6}	3.725×10^{-6}	3.650×10^{-6}	3.725×10^{-6}	3.650×10^{-6}
x_{b0}	m	1.125×10^{-6}	1.125×10^{-6}	1.125×10^{-6}	1.125×10^{-6}	1.125×10^{-6}
L_0	m	3.75×10^{-6}	3.75×10^{-6}	3.75×10^{-6}	3.75×10^{-6}	3.75×10^{-6}
$b_0 = 2\ (a_0 - y_{c0})$	m	125×10^{-9}	50×10^{-9}	200×10^{-9}	50×10^{-9}	200×10^{-9}
$(a - y_c)^{-1}$	m^{-1}	1.6×10^{7}	4.0×10^{7}	1.0×10^{7}	4.0×10^{7}	1.0×10^{7}
$(A_b/A_T)_0 \propto (x_{b0}/L_0)$	%	30	30	30	30	30
P	%	2 (1.17)	2 (0.47)	2 (1.87)	2 (0.47)	2 (1.87)
S	$m^2\ m^{-3}$	2 (1.93×10^{5})	2 (1.89×10^{5})	2 (1.98×10^{5})	2 (1.89×10^{5})	2 (1.98×10^{5})
Globular voids						
r_v	m	1.00×10^{-6}	1.00×10^{-6}	1.00×10^{-6}	1.00×10^{-6}	1.00×10^{-6}
P	%	4	4	4	4	4
S	$m^2\ m^{-3}$	1.25×10^{5}	1.25×10^{5}	1.25×10^{5}	1.25×10^{5}	1.25×10^{5}
Total						
P	%	10.4	6.6	14.0	7.01	15.46
S	$m^2\ m^{-3}$	1.20×10^{6}	1.19×10^{6}	1.21×10^{6}	1.36×10^{6}	1.39×10^{6}

Table 6
Additional material property input data for the constrained sintering model (see Part I for other material property data).

	Units		Source
E_{av}	Pa	20×10^{9}	[22]
v	–	0.25	[30]
α_{coat}	$°C^{-1}$	9×10^{-6}	[31]
$\alpha_{subs\ (Ni)}$	$°C^{-1}$	11×10^{-6}	[31]

4.2. Microstructural changes during sintering

The behaviour is, of course, dependent on the way that the microstructure evolves, although only the densifying mechanisms (occurring via grain boundary diffusion) contribute to the shrinkage represented in Fig. 3. Some insights into the way that the microstructure evolves, and the effect of the presence of a substrate, can be obtained from the predictions presented in Fig. 4, which refer to a coating with a stiffness of 10 GPa, being heat treated at 1400 °C. For a free-standing coating, both the radius of the modelled domain, r_s, and the microcrack separation, a, decrease with time (leading to in-plane shrinkage). However, in a coating attached to a zirconia substrate, splats expand in the in-plane directions (r_s increases) – see Fig. 4a. This occurs via a reversal of the direction of grain boundary diffusion, allowing through-thickness cracks to rearrange so as to relax the stress, leading to a reduction of a – see Fig. 4b. With a nickel substrate, on the other hand, both the radius of the modelled domain, r_s and the microcrack separation, a, initially increase, in order to relax the thermal expansion mismatch strain, but after this has happened r_s continues to expand, allowing a to shrink, in a similar manner to the zirconia substrate case. This reversal of grain boundary diffusion when a substrate is present results in enhanced reduction of the height of the modelled domain, h and to hence faster through-thickness shrinkage – see Fig. 4c. It can be seen in Fig. 4d that the overall porosity level initially increases on a Ni substrate, due to this microcrack opening, although in general the changes in porosity are small and are not strongly affected by attachment to a substrate (and hence would be very difficult to detect experimentally).

The initial transients being more rapid with the Ni substrate is due to the presence of relatively high initial (differential thermal expansion) stresses in that case. However, it is important to note that, while the presence of the substrate inhibits in-plane shrinkage, it does not influence non-densifying sintering mechanisms. These depend on surface diffusion, and they reduce the surface area without causing densification. For these zirconia coatings, under the conditions of interest, surface diffusion plays an important role in controlling many of the microstructural changes, and those predominantly induced by it take place in a similar manner for detached and bonded coatings. For

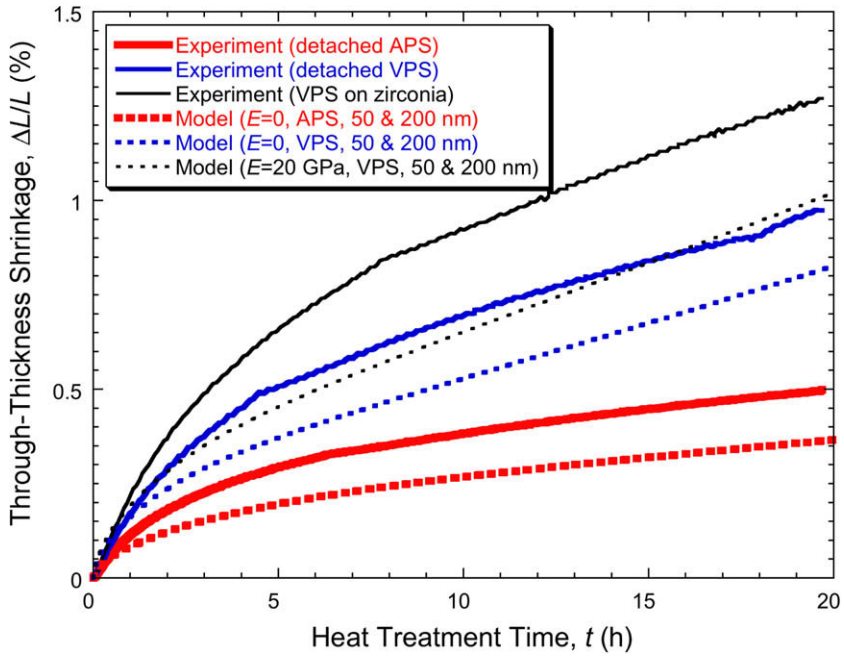

Fig. 3. Comparison between experimental data and model predictions for the through-thickness coating shrinkage at 1400 °C, for detached ($E = 0$) APS and VPS coatings, and for VPS coatings attached to a (dense) zirconia substrate. The model predictions are based on a bimodal distribution (50 and 200 nm) for the initial open dimension of both inter-splat pores and microcracks. Other microstructural parameters are those appropriate for the two types of coating – see Table 5.

example, the reduction in surface area with time, and the growth rate of the inter-splat contact area, are predicted to be very similar for free-standing coatings (see Figs. 5a and 6a of Part I) and for coatings bonded to zirconia or nickel substrates.

4.3. Relaxation of in-plane elastic stresses

Fig. 5 shows how in-plane stresses change during sintering, for coatings on zirconia and nickel substrates, and for two different coating stiffnesses. It can be seen that, on a zirconia substrate (zero stress initially), there is actually an increase in stress level in the early stages, as microstructural changes occur which would have led to shrinkage in a free-standing coating. However, these stresses subsequently become relaxed, as the driving force for (densifying) sintering becomes reduced and a quasi-steady state is established, with low levels of in-plane stress. With a nickel substrate, on the other hand, relatively high (differential thermal expansion) stresses are present from the start, so relaxation occurs from the start and leads to a quasi-steady state similar to that on the zirconia substrate. These are diffusion-driven stress relaxation phenomena (Coble creep and microcrack opening), which are a consequence of the reversal of the diffusion along grain boundaries. It is clear that, at these relatively high temperatures, this occurs quite rapidly in these coatings. Of course, the pore architecture is fine, so diffusion distances are short. Consequently, these stresses, both from differential thermal expansion and from sintering shrinkage (see Fig. 2), tend to become quickly relaxed (i.e. substantial relaxation in less than an hour) at these high temperatures.

4.4. Stored elastic strain energy and interfacial debonding (coating spallation)

An issue of practical importance is that of whether the stored energy associated with (in-plane) elastic strains is likely to be sufficient to cause spallation. Microstructural features of the interface, including its roughness, phases present in the vicinity (such as thermally grown oxides and intermetallics), defects such as porosity, microcracks, etc. are all likely to affect the ease of interfacial crack growth (i.e. the interfacial fracture energy). However, analysing local stress and strain fields in the vicinity of the interface, which has been the subject of numerous studies, is unlikely to yield a reliable rationale for the prediction of debonding. A potentially more fruitful approach is to recognize that the driving force for debonding will at least largely come from relaxation of stresses within the coating as interfacial cracking occurs – this is indeed how most coating spallation events are driven (and explains why thicker coatings tend to be more likely to debond). A necessary (but not sufficient) condition for spallation (at least by unstable propagation of an interfacial crack) is that the stored elastic strain energy in the coating (per unit area of interface) should be greater than the interfacial fracture energy, and this is a potentially fruitful rationale for lifetime prediction.

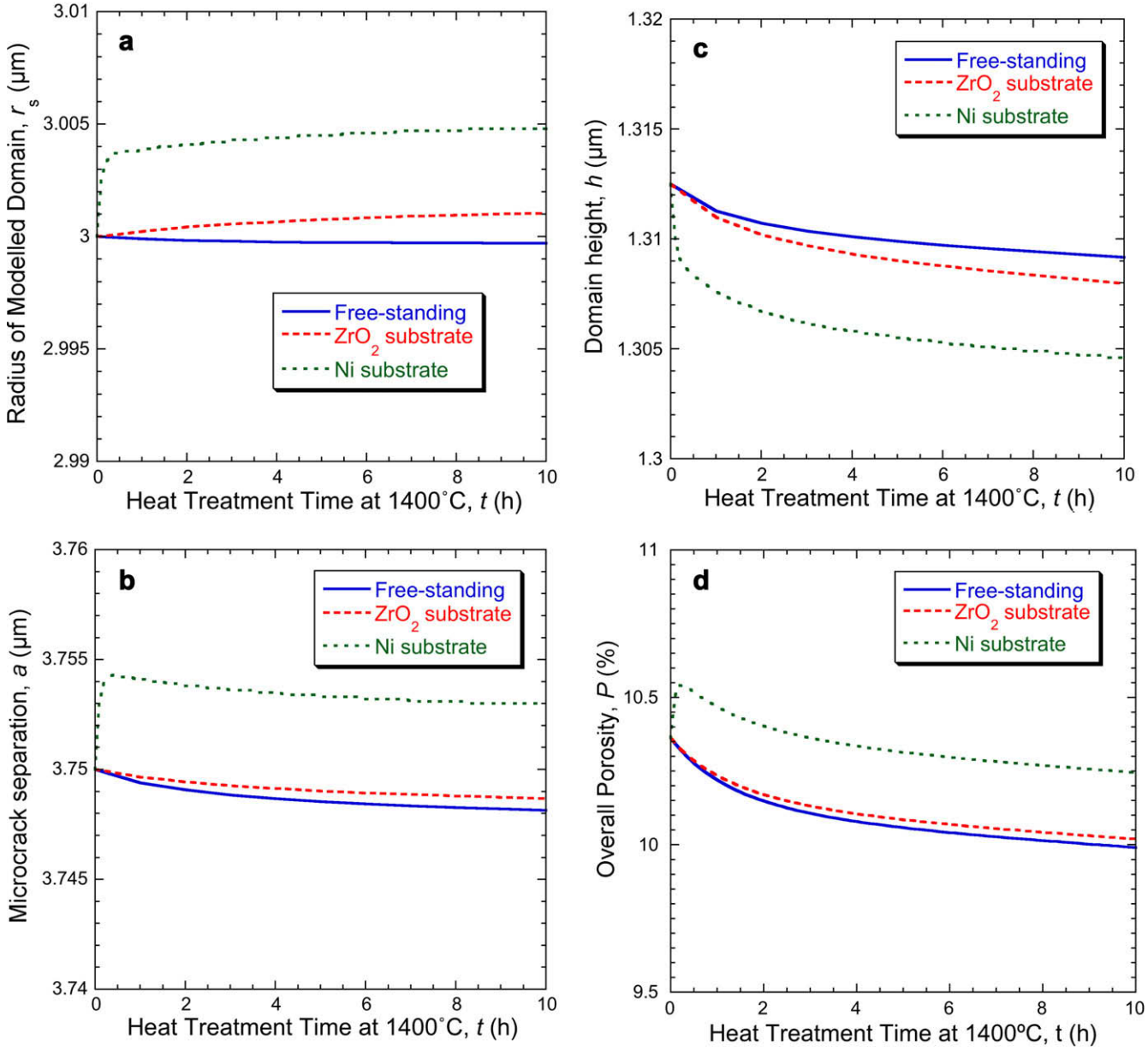

Fig. 4. Predicted evolution at 1400 °C of values of parameters representing the microstructure, for a stiffness of 10 GPa, showing (a) radius of modelled domain, r_s, (b) spacing between intra-splat microcracks, a, (c) domain height, h and (d) porosity, P.

Fig. 6 shows how the stored elastic strain energy per unit volume in the coating decreases during holding at elevated temperature, with a Ni substrate and for three different coating stiffnesses. The initial stress is due to (prior) differential thermal expansion, and clearly it is higher when the coating is stiffer. It is worth noting that these values of U^E (in J m^{-3}) can be multiplied by the coating thickness (in m) to give the strain energy release rate for interfacial debonding (in J m^{-2}). Since interfacial fracture energies are thought [27] to be of the order of 10–100 J m^{-2} for these coatings (although admittedly likely to change with extended exposure to high temperature, as a result of thickening of the thermally grown oxide, and possibly other microstructural changes in the vicinity of the interface), it can be seen that these creep phenomena are likely to reduce the driving force for debonding below the critical range quite rapidly, even for relatively stiff coatings.

Of course, overall, the effect of sintering is still likely to be such as to promote debonding. This is because it leads to substantial stiffening of the coating. (The modelling presented here has not covered this aspect, although it would be possible to devise a model for stiffness based on a geometrical representation of the pore architecture similar to that used here.) While it is clear that stresses do get rapidly relaxed during sintering, they are regenerated (assuming substrate and coating have different expansivities) every time the system is cooled down – and indeed it is during cooling that spallation is likely to occur. The plots shown in Fig. 6 confirm that these

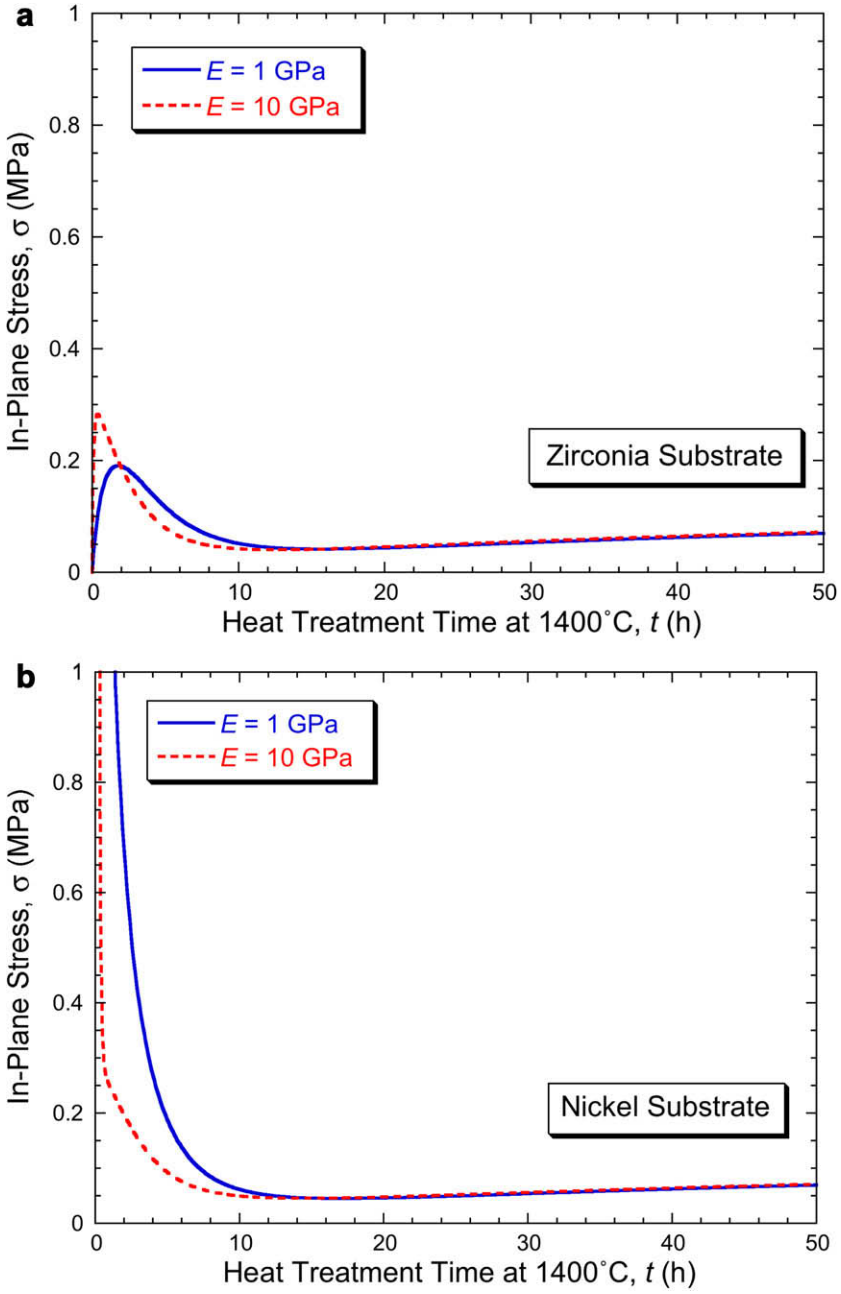

Fig. 5. Predicted changes in coating stress during heat treatment at 1400 °C, for two different coating stiffnesses, with substrates of (a) zirconia and (b) nickel.

stresses (and the associated stored elastic strain energy) can reach dangerously high levels when the coating stiffness is relatively high, although of course there is no need to model the sintering process in order to establish this. (These stresses will be compressive in the coating after cooling, whereas in the modelling presented here they are tensile – since the temperature is 1400 °C, while the stress-free temperature was taken to be 200 °C – but the magnitude of the stored elastic strain energy will be similar when this temperature change is reversed.)

The modelling results presented here indicate that attachment to a rigid substrate does not actually retard microstructural evolution (inter-splat contact area growth and surface area reduction) very substantially, since non-densifying (surface diffusion) sintering mechanisms are entirely unaffected. Nevertheless, it modifies the material redistribution (through-thickness shrinkage and in-plane expansion) so as to relax the thermal stresses. However, as mentioned above, the increased stiffness caused by sintering leads to higher stresses and stored strain energy in the coating when it is subsequently cooled, increasing the danger of spallation. Quantification of this would require a linkage between stiffness and pore architecture. It may be noted, however, that such a linkage is already in place

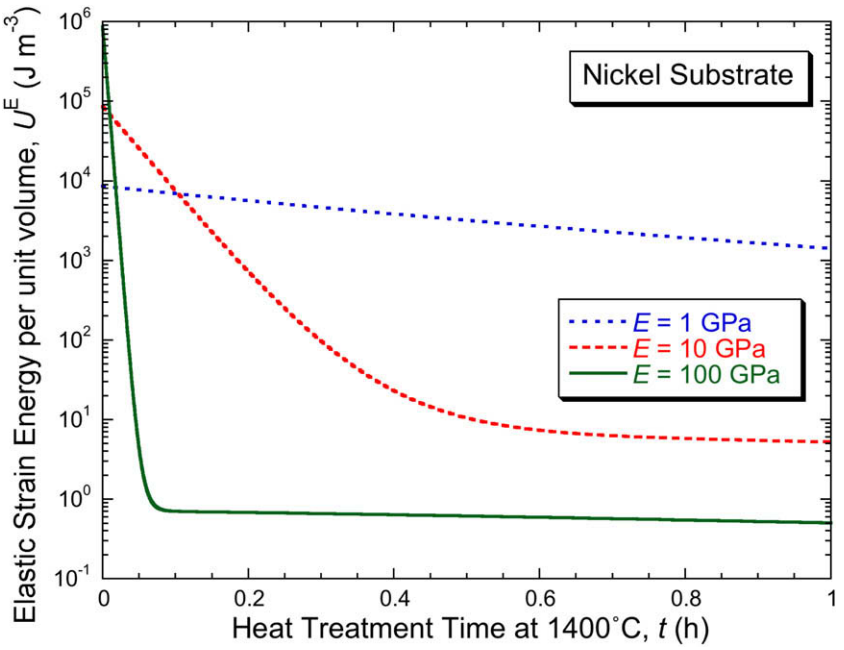

Fig. 6. Predicted changes, during heat treatment at 1400 °C, in the energy per unit volume associated with the elastic strain, for coatings of different stiffness on a Ni substrate.

for thermal conductivity [28]. One outcome of the current modelling is that increases in conductivity due to sintering are expected to occur rather similarly for detached and attached coatings. It would be helpful to explore whether this can be confirmed experimentally.

There is a further point which may turn out to be of significance. The experiments conducted here, and indeed most such experiments, are based on extended isothermal heat treatments, whereas service conditions involve thermal cycling, with rapid heating and cooling (and hence substantial through-thickness thermal gradients). Recent dilatometry experiments (on detached coatings) indicated [29] that thermal cycling retarded the rate of shrinkage (even though heating and cooling rates were relatively slow). This suggests that some form of reversal of the microstructural changes associated with sintering (e.g. rupturing of fine diffusional bridges) may arise from the stresses created during (rapid) heating and cooling, which would certainly be more pronounced under service conditions than during those experiments. This is an area requiring further work.

5. Conclusions

The following conclusions can be drawn from this work:

(a) YSZ coatings were produced on zirconia substrates by vacuum plasma spraying. Through-thickness shrinkage rates of these coatings, while attached to the substrate, were measured at elevated temperatures and compared with those of the same coatings when detached. Faster through-thickness shrinkage was observed for the attached coatings.

(b) A model, based on the variational principle, has been developed to treat the sintering of plasma-sprayed coatings, when attached to rigid substrates. In-plane elastic strains arise due to inhibition of the in-plane shrinkage associated with sintering, and also from differential thermal expansion when there are temperature changes and the substrate has a different expansivity from that of the coating. Predictions from the model are consistent with the experimentally observed shrinkage behaviour for both free-standing and attached coatings.

(c) The model has been used to explore predicted changes in pore architecture during sintering, and also the build-up and relaxation of global elastic strains and stresses. Stress relaxation occurs in the model by Coble creep and microcrack opening, as a consequence of the reversal of the diffusion along grain boundaries.

(d) Tensile stresses caused by inhibition of the (in-plane) shrinkage associated with sintering retard the densification rate. However, in the temperature range of primary interest, stress relaxation mechanisms operate relatively quickly, so that this inhibition is not very pronounced. Moreover, non-densifying (surface diffusion) sintering mechanisms are unaffected by attachment to a substrate, and these mechanisms tend to play a prominent role in the overall microstructural changes taking place. Rates of increase in thermal conductivity, and probably of stiffness, are therefore expected to occur rather similarly with free-standing and attached coatings (although it may be that progression of the microstructural

changes arising during sintering can be retarded in gas turbine engines by the stresses generated during rapid heating and cooling).

(e) While stored elastic strain energy levels in these coatings arising from (in-plane) inhibition of sintering shrinkage tend to remain low, those from differential thermal expansion can be high immediately after a temperature change, particularly after cooling to a temperature at which stress relaxation rates are slow. It has been shown that such strain energies, when converted to strain energy release rates per unit area for typical coating thicknesses, could exceed the fracture energy of the interface, and thus make spallation energetically favourable, particularly if the coating stiffness has been raised by sintering.

Acknowledgements

Financial support has come from a Basque Government scholarship (for A.C.), from EPSRC via a Platform Grant (for I.O.G.) and from Sulzer Metco (US) Inc. The authors are grateful for the extensive technical assistance of Sulzer Metco and for various useful discussions with Sulzer Metco personnel, notably Mitch Dorfman and Clive Britton.

References

[1] Cipitria A, Golosnoy IO, Clyne TW. Acta Mater 2009;57:980.
[2] Bordia RK, Raj R. J Am Ceram Soc 1985;68:287.
[3] Bordia RK, Scherer GW. Acta Metall 1988;36:2393.
[4] Bordia RK, Scherer GW. Acta Metall 1988;36:2399.
[5] Bordia RK, Scherer GW. Acta Metall 1988;36:2411.
[6] Bordia RK, Jagota A. J Am Ceram Soc 1993;76:2475.
[7] Scherer GW, Garino T. J Am Ceram Soc 1985;68:216.
[8] Garino TJ, Bowen HK. J Am Ceram Soc 1987;70:C315.
[9] Garino TJ, Bowen HK. J Am Ceram Soc 1990;73:251.
[10] Bordia RK, Zuo R, Guillon O, Salamone SM, Rödel J. Acta Mater 2006;54:111.
[11] Wonisch A, Guillon O, Kraft T, Moseler M, Riedel H, Rodel J, et al. Acta Mater 2007;55:5187.
[12] Green DJ, Guillon O, Rodel J. J Eur Ceram Soc 2008;28:1451.
[13] Hsueh CH. Scripta Metall 1985;19:1213.
[14] Cheng T, Raj R. J Am Ceram Soc 1989;72:1649.
[15] Lu XJ, Xiao P. J Eur Ceram Soc 2007;27:2613.
[16] Jagota A, Hui CY. Mech Mater 1991;11:221.
[17] Hutchinson RG, Fleck NA, Cocks ACF. Acta Mater 2006;54:1297.
[18] Eaton HE, Novak RC. Surf Coat Technol 1987;32:227.
[19] Ahrens M, Lampenscherf S, Vassen R, Stover D. J Thermal Spray Technol 2004;13:432.
[20] Tsipas SA, Golosnoy IO, Damani R, Clyne TW. J Thermal Spray Technol 2004;13:370.
[21] Choi SR, Zhu DM, Miller RA. J Am Ceram Soc 2005;88:2859.
[22] Paul S, Cipitria A, Golosnoy IO, Clyne TW. J Thermal Spray Technol 2007;16:798.
[23] Thompson JA, Clyne TW. Acta Mater 2001;49:1565.
[24] Pan J, Cocks ACF, Kucherenko S. Proc R Soc Lond A 1997;453:2161.
[25] Cocks ACF, Gill SPA, Pan J. Adv Appl Mech 1999;36:81.
[26] Pan J. Int Mater Rev 2003;48:69.
[27] Tsui YC, Clyne TW. Adhesion of thermal barrier coating systems and incorporation of an oxidation barrier layer. In: Berndt CC, editor. Thermal spray: practical solutions for engineering problems. Proceedings of the 9th national thermal spray conference. Cincinatti, OH: ASM; 1996. p. 275.
[28] Golosnoy IO, Tsipas SA, Clyne TW. J Thermal Spray Technol 2005;14:205.
[29] Paul S, Cipitria A, Tsipas SA, Clyne TW. Surf Coat Technol 2009;203:1069.
[30] German RN. Sintering theory and practice. New York: John Wiley; 1996.
[31] Evans AG, Mumm DR, Hutchinson JW, Meier GH, Pettit FS. Prog Mat Sci 2001;46:505.